

Chiral Ruthenium Halide Semiconductor with Strong Antiferromagnetic Coupling

Haolin Lu, Tengfei He, Haolin Wu, Fenglian Qi, Hebin Wang, Bing Sun, Tianyin Shao, Tianjiao Qiao, Hao-Li Zhang, Dali Sun, Yongsheng Chen, Zhiyong Tang, and Guankui Long*

Chiral hybrid organic–inorganic metal halides have attracted wide attention owing to their superior chiroptoelectronic and chirospintronic properties. Here, a new class of chiral lead-free metal halides, $(R/S\text{-MBA})_3\text{Ru}_2\text{Br}_9$ (MBA = methylbenzylammonium), with unique magnetic properties is reported. $(R/S\text{-MBA})_3\text{Ru}_2\text{Br}_9$ is composed of a surface-shared octahedron dimer separated by chiral cations and crystallizes into the *Sohncke* space group of $P2_12_12_1$. The crystal structures, chiroptical, magnetic properties, and magnetic circular dichroism of $(R/S\text{-MBA})_3\text{Ru}_2\text{Br}_9$ are systematically investigated. Owing to the strong antiferromagnetic coupling between the Ru atom through bromine bridge in the $[\text{Ru}_2\text{Br}_9]^{3-}$ dimer and the weak ferromagnetic coupling between the neighboring $[\text{Ru}_2\text{Br}_9]^{3-}$ dimer, $(R/S\text{-MBA})_3\text{Ru}_2\text{Br}_9$ exhibits antiferromagnetic property with Néel temperature at 7 K. Considering the unique magnetic property of ruthenium, together with the rapid progress of antiferromagnetic spintronics and optospintronics recently, this work provides a novel multifunctional lead-free chiral magnetic candidate toward chiral optoelectronics and antiferromagnetic spintronics.

in chiral optoelectronic^[4] and chirospintronic devices.^[5] Chiroptical properties such as circular dichroism (CD), circularly polarized luminescence,^[6] and nonlinear chiroptical effects^[7] were reported based on these chiral HOIMHs. Then, circularly polarized photodetectors^[8] and spin light-emitting diodes^[5b,9] based on the unique chiral optoelectronic and spintronic properties of chiral HOIMHs were demonstrated.^[10]

Due to the toxicity of lead, people have been looking for the alternative lead-free chiral HOIMHs for a long time. For example, the neighbors of Pb in the periodic table of elements, such as Sb and Bi, were employed directly or combined with monovalent metal cations (such as Ag) to construct the lead-free chiral HOIMHs.^[11] Therefore, lead-free chiral perovskite-derived structures and related compounds with formulas of $\text{A}_2\text{M}(\text{I})\text{M}(\text{III})\text{X}_6$ and

$\text{A}_3\text{M}(\text{III})_2\text{X}_9$ were received wide research interest. However, the current research mainly focuses on the nonmagnetic systems such as group VA metal halides, and it is highly needed to combine chirality with the superior magnetic and spintronic properties of perovskites.

1. Introduction

Combining chirality with the remarkable optical,^[1] electrical,^[2] and spintronic properties^[3] of perovskites, chiral hybrid organic–inorganic metal halides (HOIMHs) have received wide attention

H. Lu, T. He, H. Wu, H. Wang, T. Shao, T. Qiao, G. Long
School of Materials Science and Engineering, Tianjin Key Lab for Rare Earth Materials and Applications
Smart Sensing Interdisciplinary Science Center
Renewable Energy Conversion and Storage Center (RECAST)
Nankai University
Tianjin 300350, China
E-mail: longgk09@nankai.edu.cn

T. He, Y. Chen
The Centre of Nanoscale Science and Technology and Key Laboratory of Functional Polymer Materials
Institute of Polymer Chemistry
Renewable Energy Conversion and Storage Center (RECAST)
College of Chemistry
Nankai University
Tianjin 300071, China

F. Qi, Z. Tang
Chinese Academy of Science (CAS) Key Laboratory of Nanosystem and Hierarchy Fabrication
CAS Center for Excellence in Nanoscience
National Center for Nanoscience and Technology
Beijing 100190, China

B. Sun, H.-L. Zhang
State Key Laboratory of Applied Organic Chemistry (SKLAOC)
Key Laboratory of Special Function Materials and Structure Design (MOE)
College of Chemistry and Chemical Engineering
Lanzhou University
Lanzhou 730000, China

D. Sun
Department of Physics
North Carolina State University
Raleigh, NC 27695-8202, USA

 The ORCID identification number(s) for the author(s) of this article can be found under <https://doi.org/10.1002/adfm.202308862>

DOI: 10.1002/adfm.202308862

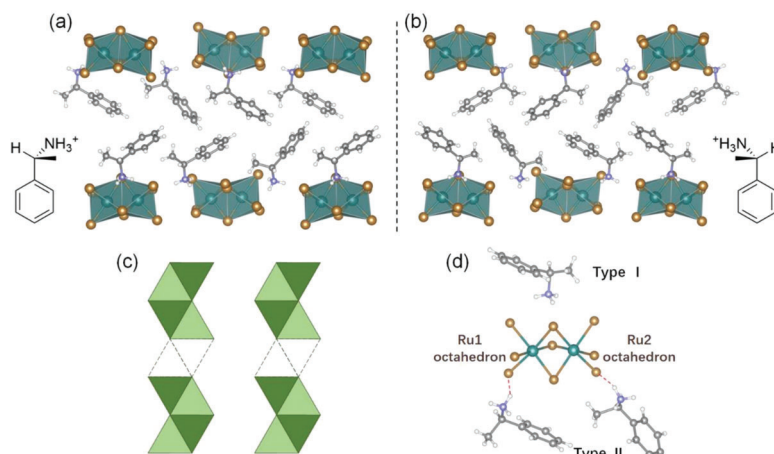


Figure 1. Packing views of the crystal structures of a) $(R\text{-MBA})_3\text{Ru}_2\text{Br}_9$ and b) $(S\text{-MBA})_3\text{Ru}_2\text{Br}_9$. Ru, C, H, N, and Br atoms are colored with green, gray, white, blue, and brown, respectively. c) Schematic diagram of a vacancy ordered perovskite structure. d) Two types of distributions of organic cations around the $[\text{Ru}_2\text{Br}_9]^{3-}$ dimer, and hydrogen bonds are shown. The face-shared octahedra are named as “Ru1 octahedron” and “Ru2 octahedron”.

Recently, ruthenium-based perovskites have attracted wide research interest. Ruthenium oxide perovskites, such as 3D ARuO_3 ($A = \text{Ca, Sr or Ba}$) and Ruddlesden–Popper type $\text{A}_{n+1}\text{Ru}_n\text{O}_{3n+1}$ perovskites ($A = \text{Ca, Sr or Ba}$; $n = 1, 2 \text{ or } 3$), exhibit excellent magnetic and spintronic properties, such as spin-triplet superconductivity, coexistence of ferromagnetism and metal conductivity.^[12] Cheetham and co-workers recently reported a series of Ru-based hybrid perovskites and metal halides, and found their optical and magnetic properties can be tuned by the A-site engineering.^[13] However, most of the reported Ru-based metal halides are based on the inorganic cations (such as M_2RuX_6 , $\text{M} = \text{K, Rb, Cs}$, $\text{X} = \text{Cl or Br}$), and there are only few reports on organic cations.^[13a,14] Most importantly, the chiral Ru-based HOIMHs have not been reported.

In this work, we extended the research field of chiral metal halides to Ru-related compounds and synthesized the Ru-based chiral HOIMH, $(R/S\text{-MBA})_3\text{Ru}_2\text{Br}_9$ (MBA = methylbenzylammonium). The chiroptical and magnetic properties of $(R/S\text{-MBA})_3\text{Ru}_2\text{Br}_9$ were systematically investigated by both experimental investigation and theoretical calculation, and found that chirality is successfully incorporated into the inorganic framework. Owing to the strong antiferromagnetic coupling between the Ru atom through bromine bridge in the $[\text{Ru}_2\text{Br}_9]^{3-}$ dimer, $(R/S\text{-MBA})_3\text{Ru}_2\text{Br}_9$ exhibits strong antiferromagnetic nature with significantly decreased effective magnetic moment. Considering the unique magnetic property of ruthenium, together with rapid progress of antiferromagnetic spintronics^[15] and optospintronics^[16] recently, our work provides a novel multifunctional lead-free chiral magnetic candidate toward chiral optoelectronics and antiferromagnetic spintronics.

2. Results and Discussion

One of the typical idealized perovskite-derived structures is the vacancy ordered surface shared hexagonal structure derived from BaNiO_3 .^[13a] The $(R/S\text{-MBA})_3\text{Ru}_2\text{Br}_9$ single crystal was synthesized by the hydrothermal method, and their crystal structures

are shown in **Figure 1a,b**, which is the representative of the above-mentioned structural series. $(R/S\text{-MBA})_3\text{Ru}_2\text{Br}_9$ crystallizes into the $P2_12_12_1$ Sohncke space group, and $[\text{Ru}_2\text{Br}_9]^{3-}$ dimer is formed by two $[\text{RuBr}_6]^{3-}$ octahedrons through face sharing (Figure 1c). There are two types of contact between the chiral cations and $[\text{Ru}_2\text{Br}_9]^{3-}$ dimer: one type of chiral cation is distributed near the shared surface of the dimer (Type I in Figure 1d), and the other type is distributed near the terminal of the $[\text{Ru}_2\text{Br}_9]^{3-}$ dimer through hydrogen bonding (Type II in Figure 1d). The powder X-ray diffraction patterns of $(R\text{-MBA})_3\text{Ru}_2\text{Br}_9$ and $(S\text{-MBA})_3\text{Ru}_2\text{Br}_9$ exhibit sharp peaks and identical features with the simulated XRD based on their single crystals, which confirm the phase purity of the as-synthesized crystals (Figure S1, Supporting Information). Thermogravimetric analysis indicates that $(R\text{-MBA})_3\text{Ru}_2\text{Br}_9$ and $(S\text{-MBA})_3\text{Ru}_2\text{Br}_9$ possess high thermal stability, with identical decomposition temperatures of 246 °C (Figure S2, Supporting Information).

Due to the chiral induction effect by the MBA cation as well as the hydrogen bond between the chiral cations and inorganic framework, the $[\text{RuBr}_6]$ octahedrons in $(R/S\text{-MBA})_3\text{Ru}_2\text{Br}_9$ are more distorted. Similar phenomenon has been widely observed in other chiral metal halides.^[17] For instance, the Ru–Br bond lengths in $\text{MA}_3\text{Ru}_2\text{Br}_9$ are symmetric (as shown in Figure S3a, Supporting Information),^[13a] while the Ru–Br bond lengths in $(R\text{-MBA})_3\text{Ru}_2\text{Br}_9$ and $(S\text{-MBA})_3\text{Ru}_2\text{Br}_9$ are diverse from each other (as shown in **Figure 2a** and Figure S3b (Supporting Information)), which indicate the distortion degree of the inorganic dimer increases with the introduction of chiral cations.

To quantify the bond length distortion in the $[\text{Ru}_2\text{Br}_9]^{3-}$ dimers, the bond length distortion index (D) is calculated based on Equation (1)

$$D = \frac{1}{n} \sum_{i=1}^n \frac{|d_i - d_0|}{d_0} \quad (1)$$

where d_i represents the length of the Ru–Br bond and d_0 is the averaged Ru–Br bond length. As shown in Figure 2b, the bond length distortion index of $(R/S\text{-MBA})_3\text{Ru}_2\text{Br}_9$ is much larger

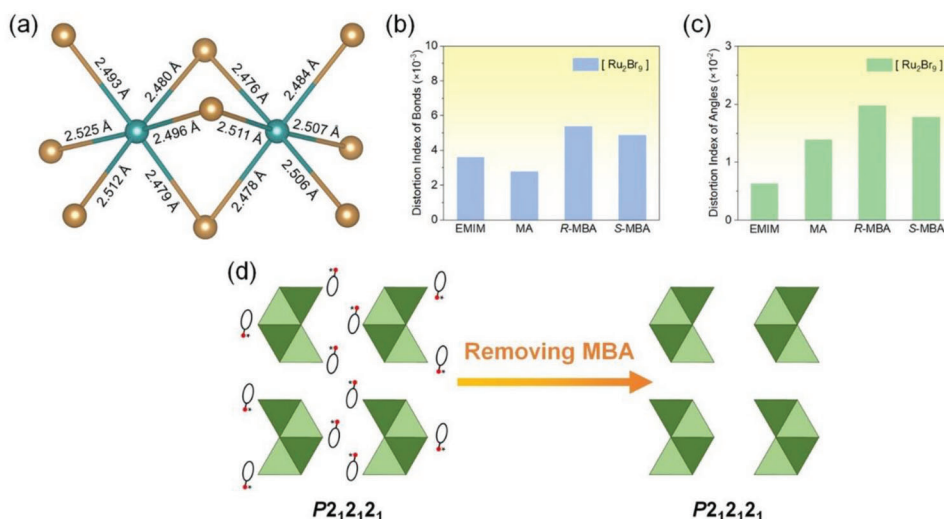


Figure 2. a) Ball-and-stick model of $(R\text{-MBA})_3\text{Ru}_2\text{Br}_9$ showing the bond lengths and connectivity in the $[\text{Ru}_2\text{Br}_9]^{3-}$ dimer. The calculated distortion index of b) bond length and c) bond angle of $(\text{EMIM})_3\text{Ru}_2\text{Br}_9$, $\text{MA}_3\text{Ru}_2\text{Br}_9$, $(R\text{-MBA})_3\text{Ru}_2\text{Br}_9$, and $(S\text{-MBA})_3\text{Ru}_2\text{Br}_9$. d) The structure diagram of chiral $\text{MBA}_3\text{Ru}_2\text{Br}_9$ without organic cations.

than that of $\text{MA}_3\text{Ru}_2\text{Br}_9$ (MA = methylammonium)^[13a] and $(\text{EMIM})_3\text{Ru}_2\text{Br}_9$ (EMIM = 1-ethyl-3-methylimidazolium).^[14b] To further quantify the distortion degree of the octahedron, the distortion index (σ) of the bond angle is further calculated based on Equation (2)

$$\sigma = \frac{1}{n} \sum_{i=1}^n \frac{|\theta_i - 90^\circ|}{90^\circ} \quad (2)$$

where θ_i represents the Br–Ru–Br bond angle in the $[\text{Ru}_2\text{Br}_9]^{3-}$ dimer. As shown in Figure 2c, the bond angle of $(R/S\text{-MBA})_3\text{Ru}_2\text{Br}_9$ also deviates more from 90° than that of $\text{MA}_3\text{Ru}_2\text{Br}_9$ ^[13a] and $(\text{EMIM})_3\text{Ru}_2\text{Br}_9$.^[14b] This is attributed to the distortion of the inorganic skeleton by the induction of chiral organic cations. On the other hand, since the face-shared $[\text{RuBr}_6]^{3-}$ octahedra in $[\text{Ru}_2\text{Br}_9]^{3-}$ are not equivalent (Figure 2a; Figure S3, Supporting Information), the distortion indices of bond length and bond angle of each octahedra are also calculated (as shown in Figure S5, Supporting Information). It is found the distortion indices of each $[\text{RuBr}_6]^{3-}$ octahedra increase as the average distance between its Br atoms and the adjacent ammonium decrease (as shown in Figures S6 and S7, Supporting Information). Most importantly, the space group of the inorganic skeletons of $(R/S\text{-MBA})_3\text{Ru}_2\text{Br}_9$ after removing the chiral cations is still $P2_12_12_1$ (Figure 2d; Figure S8, Supporting Information),^[18] which indicates that chirality is successfully transferred to the inorganic skeleton through chiral induction by the chiral cations. The Wilson statistics and cumulative intensity distributions of the X-ray reflections (Figures S9 and S10, Supporting Information) further confirm this conclusion and $(R\text{-MBA})_3\text{Ru}_2\text{Br}_9$ exhibits more acentric characteristics than $(S\text{-MBA})_3\text{Ru}_2\text{Br}_9$.

The chirality of the $(R\text{-MBA})_3\text{Ru}_2\text{Br}_9$ and $(S\text{-MBA})_3\text{Ru}_2\text{Br}_9$ was firstly investigated vibrational circular dichroism (VCD) and Fourier transform infrared spectroscopy (FT-IR). As shown in Figure 3, the VCD spectra of $(R\text{-MBA})_3\text{Ru}_2\text{Br}_9$ and

$(S\text{-MBA})_3\text{Ru}_2\text{Br}_9$ confirmed their enantiomeric nature. There are several pairs of obvious VCD peaks ($\Delta\epsilon$) at 1160 and 1223 cm^{-1} , which are attributed to the C–N vibrational mode associated with the chiral center of organic cations. Due to the heavy atomic masses of Ru and Br atoms thus the larger reduced mass, the characteristic infrared and VCD peaks of $[\text{Ru}_2\text{Br}_9]^{3-}$ are in the region of 200–300 cm^{-1} , which are out of the of normal VCD and FT-IR measuring range (Figure S11, Supporting Information). Thus, to further identify the chirality transfer, the absorption spectra, circular dichroism, and frontier molecular orbital of $(R\text{-MBA})_3\text{Ru}_2\text{Br}_9$ and $(S\text{-MBA})_3\text{Ru}_2\text{Br}_9$ are investigated by combining both experiments with theoretical calculation.

The optical properties of $(R/S\text{-MBA})_3\text{Ru}_2\text{Br}_9$ powder in KBr plates were measured, and they exhibit a typical absorption peak at ≈ 510 nm (Figure 4a). In order to better understand the origin

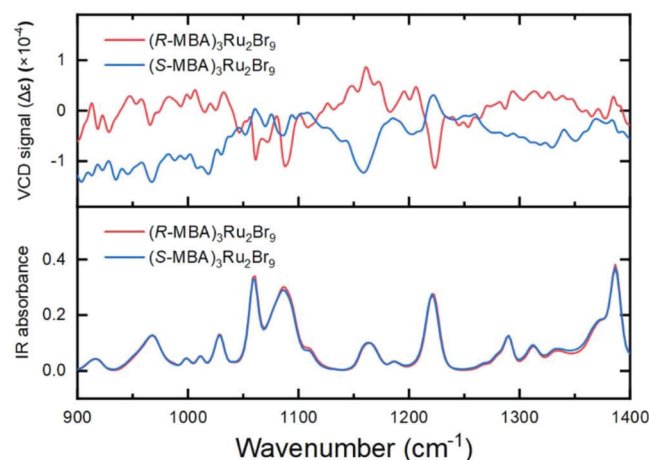


Figure 3. Experimentally measured VCD and FT-IR spectra for $(R/S\text{-MBA})_3\text{Ru}_2\text{Br}_9$.

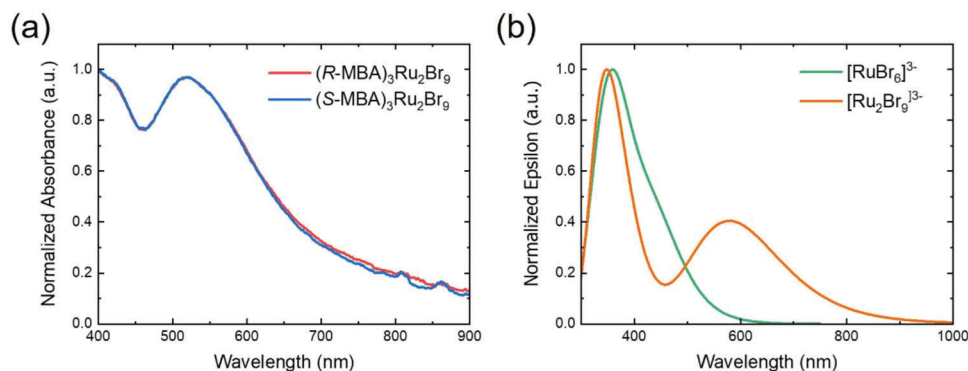


Figure 4. a) The absorbance spectra of $(R/S\text{-MBA})_3\text{Ru}_2\text{Br}_9$ powder. b) The calculated absorption spectra of $[\text{RuBr}_6]^{3-}$ and $[\text{Ru}_2\text{Br}_9]^{3-}$.

of these absorption peaks, the absorption spectra of mononuclear $[\text{RuBr}_6]^{3-}$ and binuclear $[\text{Ru}_2\text{Br}_9]^{3-}$ were calculated based on the time-dependent density functional theory. As shown in Figure 4b, the calculated absorption spectrum of $[\text{Ru}_2\text{Br}_9]^{3-}$ is in generally consistent with the shape of experimental absorption spectra of $[\text{Ru}_2\text{Br}_9]^{3-}$ in solution^[19] and the $(R/S\text{-MBA})_3\text{Ru}_2\text{Br}_9$ powder. Besides the absorption peak at 350 nm (peak I), an additional peak (peak II) arises in $[\text{Ru}_2\text{Br}_9]^{3-}$.

With the aid of natural transition orbital (NTO) analysis as shown in Figure 5a, it is obvious that peak I is mainly dominated by the ligand-to-metal charge transfer. The additional peak at 500–700 nm (peak II) arises in $[\text{Ru}_2\text{Br}_9]^{3-}$ should be ascribed to the metal–metal interaction since the orbitals involved in this optical transition exhibit large contribution from the d_{z^2} of the two adjacent Ru atoms (Figure 5b). As previously reported, two approaching low spin d^5 centers will induce energy level splitting and rearranging (Figure S13, Supporting Information). Thus, the two adjacent d_{z^2} orbitals are interacted, leading to the specific $\sigma \rightarrow \sigma^*$ transition between the two bonded octahedrons, which contributes to the absorption peak II. Most importantly, the CD spectra also show obviously polarized absorption signals with opposite sign at peak II (≈ 500 and 680 nm) for $(R\text{-MBA})_3\text{Ru}_2\text{Br}_9$ and $(S\text{-MBA})_3\text{Ru}_2\text{Br}_9$ (as

shown in Figure S12, Supporting Information). Therefore, combining the above analysis and CD spectra, peak II corresponds to the metal–metal interaction, and chirality is successfully transferred from chiral organic cations to the inorganic $[\text{Ru}_2\text{Br}_9]^{3-}$ dimer.

Then, the magnetic properties of the $(R\text{-MBA})_3\text{Ru}_2\text{Br}_9$ and $(S\text{-MBA})_3\text{Ru}_2\text{Br}_9$ powders were investigated by using the superconducting quantum interference device—vibrating sample magnetometer (SQUID-VSM). The temperature-dependent magnetic susceptibility from 2 to 300 K is measured and shown in Figure 6a. With the decrease of temperature, the magnetic susceptibility gradually increases, peaking at ≈ 9 K, and then decreases significantly. This indicates there is strong antiferromagnetic interaction in $(R\text{-MBA})_3\text{Ru}_2\text{Br}_9$ and $(S\text{-MBA})_3\text{Ru}_2\text{Br}_9$. The product of magnetic susceptibility and temperature is then taken as the derivative of temperature, the Néel temperature (T_N) of paramagnetic to antiferromagnetic coupling of $(R\text{-MBA})_3\text{Ru}_2\text{Br}_9$ and $(S\text{-MBA})_3\text{Ru}_2\text{Br}_9$ is 7 K (as shown in the illustration of Figure 6a).

The effective magnetic moment of $(R\text{-MBA})_3\text{Ru}_2\text{Br}_9$ and $(S\text{-MBA})_3\text{Ru}_2\text{Br}_9$ as a function of temperature was then calculated (Figure 6b). The effective magnetic moment (m_{eff}) of low spin Ru^{3+} (d^5) in the octahedral environment is defined by Equation (3)^[20]

$$m_{\text{eff}}^2 = \frac{3x + 8 - 8e^{-\frac{3}{2}x}}{x(1 + 2e^{-\frac{3}{2}x})} \quad (3)$$

where $\chi = \xi/k_B T$ and ξ is the strength of spin–orbit coupling. As previously reported,^[13a] the spin–orbit coupling constant χ is taken as 610 cm^{-1} .^[21] The theoretical correlation between m_{eff} and $k_B T/\xi$ of the low-spin Ru^{3+} (d^5) ion is shown in Figure 6b (black solid line). The effective magnetic moment of Ru^{3+} in $(R/S\text{-MBA})_3\text{Ru}_2\text{Br}_9$ deviates significantly from the ideal behavior curve of the Ru^{3+} ion, regardless of the value of the spin–orbit coupling constant. This should be attributed to the strong antiferromagnetic coupling between the Ru atom through bromine bridge in the $[\text{Ru}_2\text{Br}_9]^{3-}$ dimer, as previously speculated.

In order to better understand the magnetic behavior of $(R/S\text{-MBA})_3\text{Ru}_2\text{Br}_9$, the spin density of the isolated $[\text{RuBr}_6]^{3-}$ ion and $[\text{Ru}_2\text{Br}_9]^{3-}$ dimer in $(R\text{-MBA})_3\text{Ru}_2\text{Br}_9$ is calculated (as shown

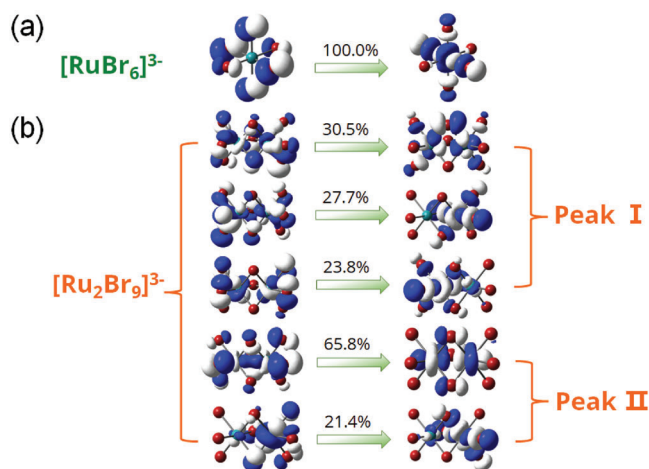


Figure 5. The calculated NTO of a) $[\text{RuBr}_6]^{3-}$ and b) $[\text{Ru}_2\text{Br}_9]^{3-}$.

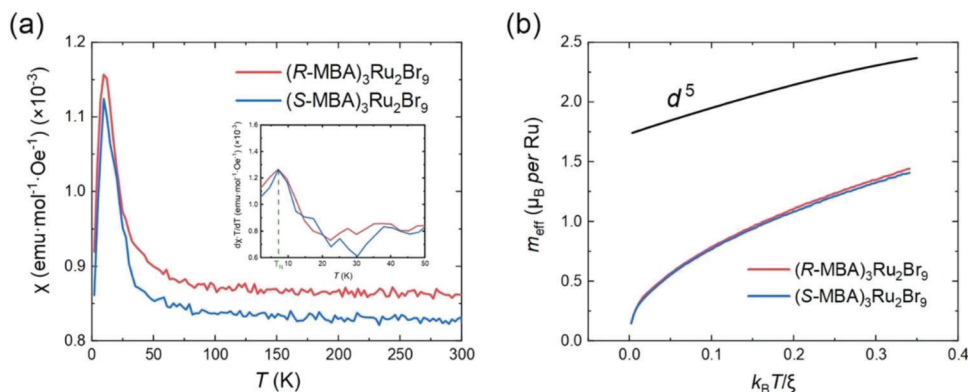


Figure 6. Magnetic properties of $(R/S\text{-MBA})_3\text{Ru}_2\text{Br}_9$. a) The temperature dependence of the magnetic susceptibility of $(R\text{-MBA})_3\text{Ru}_2\text{Br}_9$ and $(S\text{-MBA})_3\text{Ru}_2\text{Br}_9$ in an applied magnetic field of 500 Oe. The inset shows the product of magnetic susceptibility and temperature as the derivative of temperature of $(R/S\text{-MBA})_3\text{Ru}_2\text{Br}_9$, and the Néel temperature (T_N) is 7 K. b) The experimental Kotani plots for $(R\text{-MBA})_3\text{Ru}_2\text{Br}_9$ and $(S\text{-MBA})_3\text{Ru}_2\text{Br}_9$. The theoretical Kotani plots for Ru^{3+} (d^5) ion are given as black line for comparison.

in **Figure 7**; Figure S14, Supporting Information). The calculated spin density of isolated $[\text{RuBr}_6]^{3-}$ ion is $1e$ per Ru atom, which decreases significantly to $0.0001e$ per Ru atom in $(R\text{-MBA})_3\text{Ru}_2\text{Br}_9$ at 0 K. This is consistent with the experimental results as shown above, the spin arrangement of the adjacent Ru atoms in $[\text{Ru}_2\text{Br}_9]^{3-}$ is antiparallel. Thus, $(R/S\text{-MBA})_3\text{Ru}_2\text{Br}_9$ exhibits strong antiferromagnetic coupling with significantly decreased effective magnetic moment at low temperature.

To further investigate the coupling between antiferromagnetism and chirality in $(R/S\text{-MBA})_3\text{Ru}_2\text{Br}_9$, the magnetic circular dichroism (MCD) measurement is carried out. As shown in **Figure 8** and Figure S6 (Supporting Information), the intensity of MCD peak at ≈ 680 nm increases significantly with applying the positive magnetic field for $(R\text{-MBA})_3\text{Ru}_2\text{Br}_9$ and negative magnetic field for $(S\text{-MBA})_3\text{Ru}_2\text{Br}_9$, indicating the chiroptical property of antiferromagnetic chiral perovskite can also be modulated through applying the external magnetic field.^[22] Considering the rapid progress of antiferromagnetic spintronics recently,^[15,16] we believe these chiral ruthenium halides could take an important role toward the application in antiferromagnetic spintronics and optospintronics.

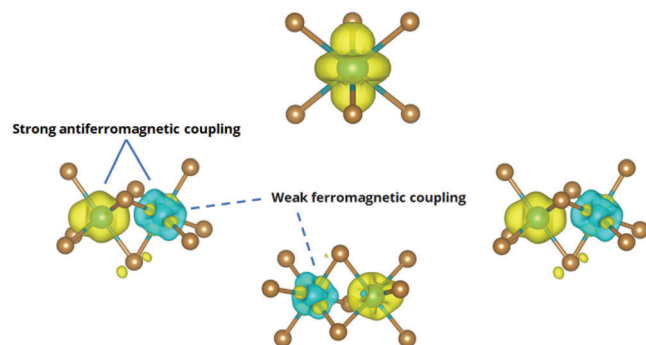


Figure 7. The calculated spin density of isolated $[\text{RuBr}_6]^{3-}$ ion and $[\text{Ru}_2\text{Br}_9]^{3-}$ dimers in $(R/S\text{-MBA})_3\text{Ru}_2\text{Br}_9$, different colors represent spin-up and spin-down.

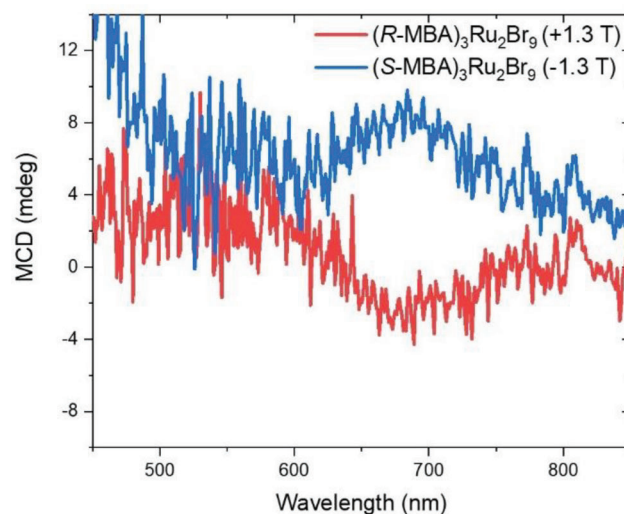


Figure 8. The MCD spectra of $(R/S\text{-MBA})_3\text{Ru}_2\text{Br}_9$.

3. Conclusion

In conclusion, we have developed a new family of chiral hybrid organic–inorganic metal halides, $(R\text{-MBA})_3\text{Ru}_2\text{Br}_9$ and $(S\text{-MBA})_3\text{Ru}_2\text{Br}_9$. They crystallize into the $P2_12_12_1$ Sohncke space group and exhibit a face-shared dimeric inorganic skeleton. As confirmed by single crystal structures, VCD, CD, and absorption spectra, together with theoretical calculation, it is confirmed the chirality is successfully transferred into the inorganic ruthenium halide skeleton. Due to the antiparallel spin arrangement between the Ru atom through bromine bridge in the $[\text{Ru}_2\text{Br}_9]^{3-}$ dimer at low temperature, these chiral ruthenium HOIMHs exhibit strong antiferromagnetic properties with Néel temperature at 7 K. Therefore, the effective magnetic moment of Ru^{3+} in $(R\text{-MBA})_3\text{Ru}_2\text{Br}_9$ and $(S\text{-MBA})_3\text{Ru}_2\text{Br}_9$ deviates significantly from the Kotani model, as confirmed by the calculated spin density. The magneto-optical response in $(R/S\text{-MBA})_3\text{Ru}_2\text{Br}_9$ was further verified by MCD. Owing to the unique magnetic property of ruthenium, our work provides a new candidate of novel

multifunctional lead-free chiral magnetic semiconductors toward application in chiral optoelectronics and antiferromagnetic spintronics.

4. Experimental Section

Experimental Details: Materials: (*R*)- α -methylbenzylamine (*R*-MBA, *ee* = 98%, Aladdin), (*S*)- α -methylbenzylamine (*S*-MBA, *ee* = 98%, Aladdin), and anhydrous RuCl₃ (97%, Bide), and 48 wt% HBr in H₂O (Macklin) were purchased from commercial sources and used as received.

Synthesis of *R/S*-MBABr: 10 mL (*R/S*)- α -methylbenzylamine was dropped into a 250 mL round bottom flask and then 25 mL HBr was slowly added into it using a constant pressure dropping funnel. Ice bath was employed to control the temperature, the solution was stirred overnight, and then evaporated at 90 °C for 3 h to obtain the *R/S*-MBABr precipitate. The precipitate was further washed three times with diethyl ether and then dried under vacuum to obtain the white solid product. The yield is \approx 50%, and the ¹H NMR and ¹³C NMR spectra of *R*- and *S*-MBABr are shown in Figures S15 and S16 of the Supporting Information. ¹H NMR (*R*-MBABr, 400 MHz, DMSO) δ 8.44 (s, 3H), 7.54 (d, *J* = 7.3 Hz, 2H), 7.48 – 7.40 (m, 2H), 7.38 (dd, *J* = 8.2, 6.1 Hz, 1H), 4.44 (dt, *J* = 12.1, 6.0 Hz, 1H), 1.53 (d, *J* = 6.8 Hz, 3H); ¹H NMR (*S*-MBABr, 400 MHz, DMSO) δ 8.41 (s, 3H), 7.51 (d, *J* = 7.1 Hz, 1H), 7.46 – 7.38 (m, 2H), 7.36 (dd, *J* = 8.2, 6.1 Hz, 1H), 4.42 (s, 1H), 1.51 (d, *J* = 6.8 Hz, 3H). ¹³C NMR (*R*-MBABr, 101 MHz, DMSO, δ): 139.22, 128.73, 128.45, 127.28, 50.04, 20.78. ¹³C NMR (*S*-MBABr, 101 MHz, DMSO, δ): 139.67, 129.18, 128.90, 127.29, 50.48, 21.23.

Synthesis of (*R/S*-MBA)₃Ru₂Br₉: A mixture of *R/S*-MBABr (404.36 mg, 2.0 mmol), RuCl₃ (207.43 mg, 1.0 mmol), and HBr (2.0 mL) was mixed and stirred overnight. Then the mixture was heated at 160 °C for 12 h in a 23 mL Teflon-lined autoclave in an oven. The autoclave was allowed to cool to room temperature, which yielded black crystals. The crystals were washed several times with dichloromethane and dried under vacuum. The yield of (*R/S*-MBA)₃Ru₂Br₉ is \approx 70%.

[CCDC 2284907 and 2213887 contains the supplementary crystallographic data for this paper. These data can be obtained free of charge from The Cambridge Crystallographic Data Centre via www.ccdc.cam.ac.uk/data_request/cif].

Supporting Information

Supporting Information is available from the Wiley Online Library or from the author.

Acknowledgements

The authors gratefully acknowledge the financial support from the NSFC (Grant Nos. 52103218, 92256202, and 12261131500), the Fundamental Research Funds for the Central Universities, Nankai University (Grant No. 023-63223021), the 111 Project (B18030), and the Opening Project of State Key Laboratory of Polymer Materials Engineering (Sichuan University) (Grant No. sklpm2021-05-02). All the theoretical calculations were performed on National Supercomputer Center in Guangzhou.

Conflict of Interest

The authors declare no conflict of interest.

Data Availability Statement

The data that support the findings of this study are available from the corresponding author upon reasonable request.

Keywords

chiral perovskite, Kotani model, magnetic property, perovskite derivative, ruthenium halide

Published online:

- a) G. Xing, N. Mathews, S. Sun, S. S. Lim, Y. M. Lam, M. Grätzel, S. Mhaisalkar, T. C. Sum, *Science* **2013**, *342*, 344; b) S. D. Stranks, H. J. Snaith, *Nat. Nanotechnol.* **2015**, *10*, 391; c) W. Cai, J. Qin, T. Pang, X. Cai, R. Jia, F. Gao, *Adv. Opt. Mater.* **2022**, *10*, 2102140; d) Z. Zhang, Z. Wang, H. H. Sung, I. D. Williams, Z. G. Yu, H. Lu, *J. Am. Chem. Soc.* **2022**, *144*, 22242; e) B. Sun, X. Liu, X. Li, Y. Zhang, X. Shao, D. Yang, H. Zhang, *Chem. Mater.* **2020**, *32*, 8914.
- a) Y. Liu, L. Collins, R. Proksch, S. Kim, B. R. Watson, B. Doughty, T. R. Calhoun, M. Ahmadi, A. V. Ievlev, S. Jesse, S. T. Retterer, A. Belianinov, K. Xiao, J. Huang, B. G. Sumpter, S. V. Kalinin, B. Hu, O. S. Ovchinnikova, *Nat. Mater.* **2018**, *17*, 1013; b) Q. Dong, Y. Fang, Y. Shao, P. Mulligan, J. Qiu, L. Cao, J. Huang, *Science* **2015**, *347*, 967; c) S. D. Stranks, G. E. Eperon, G. Grancini, C. Menelaou, M. J. P. Alcocer, T. Leijtens, L. M. Herz, A. Petrozza, H. J. Snaith, *Science* **2013**, *342*, 341; d) D. Shi, V. Adinolfi, R. Comin, M. Yuan, E. Alarousu, A. Buin, Y. Chen, S. Hoogland, A. Rothenberger, K. Katsiev, Y. Losovyj, X. Zhang, P. A. Dowben, O. F. Mohammed, E. H. Sargent, O. M. Bakr, *Science* **2015**, *347*, 519; e) K. Taniguchi, M. Nishio, N. Abe, P. J. Huang, S. Kimura, T. H. Arima, H. Miyasaka, *Angew. Chem., Int. Ed.* **2021**, *60*, 14350.
- a) C. Zhang, D. Sun, C. X. Sheng, Y. X. Zhai, K. Mielczarek, A. Zakhidov, Z. V. Vardeny, *Nat. Phys.* **2015**, *11*, 427; b) J. Wang, C. Zhang, H. Liu, R. McLaughlin, Y. Zhai, S. R. Vardeny, X. Liu, S. McGill, D. Semenov, H. Guo, R. Tsuchikawa, V. V. Deshpande, D. Sun, Z. V. Vardeny, *Nat. Commun.* **2019**, *10*, 129; c) Y. Lu, Q. Wang, R. He, F. Zhou, X. Yang, D. Wang, H. Cao, W. He, F. Pan, Z. Yang, C. Song, *Angew. Chem., Int. Ed.* **2021**, *60*, 23578.
- a) G. Long, R. Sabatini, M. I. Saidaminov, G. Lakhwani, A. Rasmita, X. Liu, E. H. Sargent, W. Gao, *Nat. Rev. Mater.* **2020**, *5*, 423; b) J. Ahn, E. Lee, J. Tan, W. Yang, B. Kim, J. Moon, *Mater. Horiz.* **2017**, *4*, 851; c) Z. N. Georgieva, B. P. Bloom, S. Ghosh, D. H. Waldeck, *Adv. Mater.* **2018**, *30*, 1800097; d) T. He, J. Li, X. Li, C. Ren, Y. Luo, F. Zhao, R. Chen, X. Lin, J. Zhang, *Appl. Phys. Lett.* **2017**, *111*, 151102; e) P.-J. Huang, K. Taniguchi, M. Shigefuji, T. Kobayashi, M. Matsubara, T. Sasagawa, H. Sato, H. Miyasaka, *Adv. Mater.* **2021**, *33*, 2008611; f) J. Wang, H. Lu, X. Pan, J. Xu, H. Liu, X. Liu, D. R. Khanal, M. F. Toney, M. C. Beard, Z. V. Vardeny, *ACS Nano* **2021**, *15*, 588.
- a) G. Long, C. Jiang, R. Sabatini, Z. Yang, M. Wei, L. N. Quan, Q. Liang, A. Rasmita, M. Askerka, G. Walters, X. Gong, J. Xing, X. Wen, R. Quintero-Bermudez, H. Yuan, G. Xing, X. R. Wang, D. Song, O. Voznyy, M. Zhang, S. Hoogland, W. Gao, Q. Xiong, E. H. Sargent, *Nat. Photonics* **2018**, *12*, 528; b) Y.-H. Kim, Y. Zhai, H. Lu, X. Pan, C. Xiao, E. A. Gaubling, S. P. Harvey, J. J. Berry, Z. V. Vardeny, J. M. Luther, M. C. Beard, *Science* **2021**, *371*, 1129.
- M. Li, Y. Wang, L. Yang, Z. Chai, Y. Wang, S. Wang, *Angew. Chem., Int. Ed.* **2022**, *61*, e202208440.
- a) C. Yuan, X. Li, S. Semin, Y. Feng, T. Rasing, J. Xu, *Nano Lett.* **2018**, *18*, 5411; b) J. Ahn, S. Ma, J.-Y. Kim, J. Kyhm, W. Yang, J. A. Lim, N. A. Kotov, J. Moon, *J. Am. Chem. Soc.* **2020**, *142*, 4206; c) B. Li, W. Rao, X. You, P. Wang, J. Wei, Z. Wei, H. Zhang, H. Cai, *Inorg. Chem.* **2023**, *62*, 942; d) H. Wang, J. Li, H. Lu, S. Gull, T. Shao, Y. Zhang, T.-F. He, Y. Chen, T. He, G. Long, *Angew. Chem., Int. Ed.* **2023**, *62*, e202309600.
- a) C. Chen, L. Gao, W. Gao, C. Ge, X. Du, Z. Li, Y. Yang, G. Niu, J. Tang, *Nat. Commun.* **2019**, *10*, 1927; b) W. Wu, L. Li, D. Li, Y. Yao, Z. Xu, X. Liu, M. Hong, J. Luo, *Adv. Opt. Mater.* **2022**, *10*, 2102678; c) Y. Zhao, M. Dong, J. Feng, J. Zhao, Y. Guo, Y. Fu, H. Gao, J. Yang, L. Jiang, Y.

- Wu, *Adv. Opt. Mater.* **2022**, *10*, 2102227; d) T. Liu, W. Shi, W. Tang, Z. Liu, B. C. Schroeder, O. Fenwick, M. J. Fuchter, *ACS Nano* **2022**, *16*, 2682.
- [9] W. Su, F. Yuan, *Sci. Bull.* **2022**, *67*, 1535.
- [10] M. K. Jana, R. Song, H. Liu, D. R. Khanal, S. M. Janke, R. Zhao, C. Liu, Z. Vally Vardeny, V. Blum, D. B. Mitzi, *Nat. Commun.* **2020**, *11*, 4699.
- [11] a) N. Dehnhardt, M. Axt, J. Zimmermann, M. Yang, G. Mette, J. Heine, *Chem. Mater.* **2020**, *32*, 4801; b) Y. Li, T. Yang, X. Liu, S. Han, J. Wang, Y. Ma, W. Guo, J. Luo, Z. Sun, *Inorg. Chem. Front.* **2020**, *7*, 2770; c) Z. Yu, S. Cao, Y. Zhao, Y. Guo, M. Dong, Y. Fu, J. Zhao, J. Yang, L. Jiang, Y. Wu, *ACS Appl. Mater. Interfaces* **2022**, *14*, 39451; d) D. Li, X. Liu, W. Wu, Y. Peng, S. Zhao, L. Li, M. Hong, J. Luo, *Angew. Chem., Int. Ed.* **2021**, *60*, 8415; e) P. K. Rajput, A. K. Poonia, S. Mukherjee, T. Sheikh, M. Shrivastava, K. V. Adarsh, A. Nag, *J. Phys. Chem. C* **2022**, *126*, 9889.
- [12] a) I. Qasim, P. E. R. Blanchard, K. S. Knight, J. Ting, B. J. Kennedy, *Dalton Trans.* **2019**, *48*, 4730; b) S. Woo, S. A. Lee, H. Mun, Y. G. Choi, C. J. Zhung, S. Shin, M. Lacotte, A. David, W. Prellier, T. Park, W. N. Kang, J. S. Lee, S. W. Kim, W. S. Choi, *Nanoscale* **2018**, *10*, 4377; c) J. Xia, W. Siemons, G. Koster, M. R. Beasley, A. Kapitulnik, *Phys. Rev. B* **2009**, *79*, 140407.
- [13] a) P. Vishnoi, J. L. Zuo, T. A. Strom, G. Wu, S. D. Wilson, R. Seshadri, A. K. Cheetham, *Angew. Chem., Int. Ed.* **2020**, *59*, 8974; b) P. Vishnoi, J. L. Zuo, J. A. Cooley, L. Kautzsch, A. Gómez-Torres, J. Murillo, S. Fortier, S. D. Wilson, R. Seshadri, A. K. Cheetham, *Angew. Chem., Int. Ed.* **2021**, *60*, 5184.
- [14] a) V. T. Coombe, G. A. Heath, T. A. Stephenson, D. K. Vattis, *J. Chem. Soc., Dalton Trans.* **1983**, 2307; b) D. Appleby, P. B. Hitchcock, K. R. Seddon, J. E. Turp, J. A. Zora, C. L. Hussey, J. R. Sanders, T. A. Ryan, *J. Chem. Soc., Dalton Trans.* **1990**, 1879.
- [15] a) T. Jungwirth, X. Marti, P. Wadley, J. Wunderlich, *Nat. Nanotechnol.* **2016**, *11*, 231; b) M. Książczyńska, V. Kinzhybalov, A. Bieńko, W. Medycki, R. Jakubas, C. Rajnák, R. Boča, A. Ozarowski, M. Ozerov, A. Piecha-Bisiorek, *Inorg. Chem. Front.* **2022**, *9*, 2353.
- [16] P. Němec, M. Fiebig, T. Kampfrath, A. V. Kimel, *Nat. Phys.* **2018**, *14*, 229.
- [17] J. Xue, Z. Wang, A. Comstock, Z. Wang, H. H. Y. Sung, I. D. Williams, D. Sun, J. Liu, H. Lu, *Chem. Mater.* **2022**, *34*, 2813.
- [18] A. Spek, *Acta Crystallogr., Sect. A: Cryst. Phys., Diffraction, Theor. Gen. Crystallogr.* **2009**, *65*, 148.
- [19] G. A. Heath, J. E. McGrady, *J. Chem. Soc., Dalton Trans.* **1994**, 3759.
- [20] M. Kotani, *J. Phys. Soc. Jpn.* **1949**, *4*, 293.
- [21] B. N. Figgis, J. Lewis, R. S. Nyholm, R. D. Peacock, *Discuss. Faraday Soc.* **1958**, *26*, 103.
- [22] R. Pan, S. Tao, K. Wang, Z.-G. Yu, *Chem. Mater.* **2023**, *35*, 1667.